ROYAL SOCIETY OF CHEMISTRY

PAPER

Gas-phase formation of silicon monoxide *via* non-adiabatic reaction dynamics and its role as a building block of interstellar silicates†

Chao He, ‡[a] Yuheng Luo, ‡[a] Srinivas Doddipatla,[a] Zhenghai Yang,[a] Tom J. Millar, [b] Rui Sun *[a] and Ralf I. Kaiser *[a]

Silicon monoxide (SiO) is classified as a key precursor and fundamental molecular building block to interstellar silicate nanoparticles, which play an essential role in the synthesis of molecular building blocks connected to the Origins of Life. In the cold interstellar medium, silicon monoxide is of critical importance in initiating a series of elementary chemical reactions leading to larger silicon oxides and eventually to silicates. To date, the fundamental formation mechanisms and chemical dynamics leading to gas phase silicon monoxide have remained largely elusive. Here, through a concerted effort between crossed molecular beam experiments and electronic structure calculations, it is revealed that instead of forming highly-stable silicon dioxide (SiO_2), silicon monoxide can be formed *via* a barrierless, exoergic, single-collision event between ground state molecular oxygen and atomic silicon involving non-adiabatic reaction dynamics through various intersystem crossings. Our research affords persuasive evidence for a likely source of highly rovibrationally excited silicon monoxide in cold molecular clouds thus initiating the complex chain of exoergic reactions leading ultimately to a population of silicates at low temperatures in our Galaxy.

Introduction

Nearly a century after the very first discovery of the silicon monoxide molecule (SiO; $X^1\Sigma^+$) in 1886 by Mabery as a product of the reduction of silicon dioxide (SiO_2) by charcoal,[1] silicon monoxide (SiO) has been classified as a key precursor and fundamental molecular building block to interstellar silicate dust – nanoparticles comprising predominantly of olivine-type ($(Mg,Fe)_2SiO_4$) refractory minerals.[2–5] These nanoparticles have been linked to the prebiotic evolution of the interstellar medium (ISM) through the synthesis of molecular precursors to life such as sugars[6,7] and amino acids[8,9] on their ice-coated surfaces in cold molecular clouds by ionizing radiation.[10] These silicates also play a central role in star formation and in the origin of Solar Systems including our own by controlling the radiation balance, providing catalytic surfaces for, *e.g.*, formation of molecular hydrogen,[11,12] and acting as a molecular feedstock for biorelevant molecules connected to the origins of life.[2] Therefore, unraveling the origin of interstellar silicates is of vital

significance to the astrochemistry, astrobiology, and astrophysics communities to understand the fundamental processes that create a visible galaxy including our own. This knowledge is further essential to decipher the impending 'life-time-paradox' since interstellar grains are believed to be faster destroyed through sputtering and interstellar shocks[4,13] than generated during the late stage of stellar evolution in circumstellar envelopes of oxygen rich Asymptotic Giant Branch (AGB) stars.[3,14–19] The inconsistency between the formation rates of a few 10^9 years in circumstellar envelopes[20] and the destruction timescales of only some 10^8 years once injected by the stellar wind into the interstellar medium[21,22] suggests that interstellar silicates should not exist. This discrepancy might be eventually solved through a critical understanding of the complex sets of elementary reactions, which lead to these nanoparticles, commencing with the simplest molecular building block of interstellar silicates – the silicon monoxide molecule (SiO; $X^1\Sigma^+$) – in circumstellar environments.[14,23–25] However, Zhukovska *et al.*[26] and Draine[27] concluded that fractions of only a few percent of the interstellar silicates originate from circumstellar envelopes with hitherto rapid molecular mass growth processes operating in the low temperature interstellar (10 K) as opposed to the hot circumstellar medium of a few 1000 K.[28,29]

However, the underlying chemical dynamics and intimate reaction mechanisms leading even to the simplest precursor of silicate grains – silicon monoxide (SiO; $X^1\Sigma^+$) – in deep space

[a] *Department of Chemistry, University of Hawaiʻi at Mānoa, Honolulu, HI 96822, USA. E-mail: ralfk@hawaii.edu, ruisun@hawaii.edu*

[b] *School of Mathematics and Physics, Queen's University Belfast, University Road, Belfast, BT7 1NN, UK*
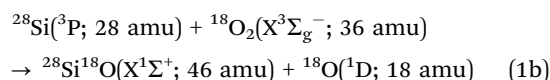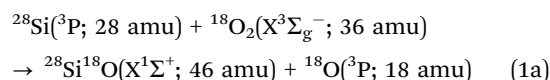
This journal is © the Owner Societies 2022

Phys. Chem. Chem. Phys., 2022, **24**, 19761–19772 | 19761

are not well understood, although this is the most abundant, silicon- and oxygen-bearing interstellar molecule contributing up to 85% of the cosmic silicon budget.[30-37] Martin *et al.*, Husain *et al.*, and Le Picard *et al.* revealed rapid kinetics of the reaction of ground state atomic silicon (Si(^{3}P)) with molecular oxygen (O$_2$, X$^3\Sigma_g^-$) down to temperatures as low as 15 K with rate constants up to 3 × 10^{-10} cm^3 s^{-1} exploiting the CRESU (Cinétique de Réaction en Écoulement Supersonique Uniforme) apparatus[38-41] albeit without an experimental identification of the reaction products or elucidation of the interplay between the triplet (reaction (1a)) *versus* singlet surfaces (reaction (1b)). Pioneering computational studies focused on the entrance channel of the singlet surface accessed through colinear and perpendicular approaches of atomic silicon to molecular oxygen, but without comprehensive searches of the intermediates involved.[42] A follow-up work tackled both the singlet and triplet surfaces, but with key reaction intermediates left out and conical intersections unexplored.[43] Two quasiclassical trajectory studies of the bimolecular collision between silicon and molecular oxygen system explored solely the ground state singlet surface and proposed a direct abstraction at low collision energy (backward scattering) and indirect reaction mechanism through insertion prevailing at high collision energies (forward–backward scattering).[44] A molecular beams study of ground state silicon with molecular oxygen determined the vibrational state distribution of silicon monoxide (SiO; X$^1\Sigma^+$) reaching a distribution maximum at ν = 4.[45] Based on the identification of ground state atomic oxygen and a significant population up to ν = 8, the authors inferred a foremost abstraction mechanism. However, the aforementioned studies did not fully appreciate the complexity of the silicon – molecular oxygen system with key reaction intermediates, conical intersections, excited state dynamics, and non-adiabatic dynamics inadequately explored. Therefore, an understanding of the chemical dynamics of the silicon – molecular oxygen system along with critical implication to interstellar silicate nano particles are still in its infancy both from the experimental and computational level.

Here, we reveal the first comprehensive results of a crossed molecular beam study merged with electronic structure calculations on the triplet and singlet surfaces of the elementary reaction of ground state atomic silicon (Si(^{3}P)) with molecular oxygen (^{18}O$_2$, X$^3\Sigma_g^-$) leading to the predominant formation of silicon monoxide (Si^{18}O; X$^1\Sigma^+$) and triplet atomic oxygen (^{18}O(^{3}P)) *via* indirect scattering dynamics. The reaction between atomic silicon (Si(^{3}P)) and molecular oxygen (^{18}O$_2$, X$^3\Sigma_g^-$) proceeds barrierlessly on the ground state singlet surface involving an unconventional cyclic intermediate, but it experiences an entrance barrier prior to the formation of an acyclic triplet Si^{18}O$_2$ reaction intermediate. Numerous intersystem crossings (ISCs) between the singlet and triplet manifold and hence non-adiabatic reaction dynamics are inferred. High level electronic structure calculations on the energies, structures, spin–orbit coupling, and conical intersections along the reaction pathways complement the molecular beams studies to reveal fundamental insights into the underlying reaction dynamics on ground and excited state surfaces and the intimate bond-breaking

and bond-formation processes along with isomerization processes of highly reactive (ring strained) intermediates. This system is also of fundamental significance to the reaction dynamics community as a benchmark of triatomic systems such as the reactions of hydrogen (H, ^{2}S),[46-48] chlorine, (Cl, ^{2}P),[49-53] fluorine (F, ^{2}P),[54-58] carbon (C, ^{1}D),[59,60] nitrogen (N, ^{2}D),[61-64] oxygen (O, ^{1}D),[65,66] and sulfur (S, ^{3}P/^{1}D)[67-69] atoms with molecular hydrogen (H$_2$, X$^1\Sigma_g^+$). However, the reaction dynamics of triatomic systems involving the 'heavy' main group XIV element silicon have been elusive until now. Our study represents a proxy for the reaction of molecular oxygen (O$_2$, X$^3\Sigma_g^-$) yielding silicon monoxide (SiO; X$^1\Sigma^+$) *via* a single collision event in the gas-phase. In cold molecular clouds, the reaction of atomic silicon with molecular oxygen initiates the formation of the very first silicon – oxygen bond and offers a viable pathway to silicon monoxide (SiO; X$^1\Sigma^+$) thus initiating the complex chain of exoergic reactions leading ultimately to a population of silicates at low temperatures in our Galaxy.

$$^{28}\text{Si}(^3\text{P}; 28 \text{ amu}) + {}^{18}\text{O}_2(\text{X}^3\Sigma_g^-; 36 \text{ amu})$$
$$\rightarrow {}^{28}\text{Si}^{18}\text{O}(\text{X}^1\Sigma^+; 46 \text{ amu}) + {}^{18}\text{O}(^3\text{P}; 18 \text{ amu}) \quad (1a)$$

$$^{28}\text{Si}(^3\text{P}; 28 \text{ amu}) + {}^{18}\text{O}_2(\text{X}^3\Sigma_g^-; 36 \text{ amu})$$
$$\rightarrow {}^{28}\text{Si}^{18}\text{O}(\text{X}^1\Sigma^+; 46 \text{ amu}) + {}^{18}\text{O}(^1\text{D}; 18 \text{ amu}) \quad (1b)$$

Methods

Experimental procedures

The bimolecular reaction of ground state atomic silicon (Si; ^{3}P) with oxygen-18 (^{18}O$_2$; X$^3\Sigma_g^-$) was carried out under single-collision conditions utilizing a universal crossed molecular beams machine.[70] In the primary source chamber, a pulsed supersonic beam of ground state silicon atoms was prepared *in situ via* ablation of silicon from a rotating silicon rod at 266 nm (Nd:YAG laser; 5 ± 1 mJ per pulse; 30 Hz)[71] and entraining the ablated atoms in neon gas (Ne; 99.999%; Specialty Gases of America) with a backing pressure of 4 atm. The neon-seeded silicon beam was skimmed and velocity-selected by a four-slot chopper wheel resulting in a peak velocity (v_p) of 952 ± 15 m s^{-1} and speed ratio (S) of 6.1 ± 0.6 (Table S1, ESI†). Laser-induced fluorescence interrogation of neon-seeded silicon beam revealed that all silicon atoms are populated in their electronic ground state (^{3}P).[72] In the secondary source chamber, the supersonic beam of oxygen-18 (^{18}O$_2$, ≥99.9%; Linde Electronics and Specialty Gases), which was characterized with v_p = 760 ± 20 m s^{-1} and S = 13.8 ± 1.0 (Table S1, ESI†), crossed perpendicularly with the primary beam silicon atoms in the interaction region yielding a collision energy (E_C) of (11.9 ± 3.0) kJ mol^{-1} and a center of mass angle (Θ_{CM}) of (46.5 ± 1.2)°. The neutral reaction products entering the detector were ionized by electron impact ionizer (80 eV, 2.0 mA),[73] then filtered according to the mass-to-charge ratio (m/z) utilizing a quadrupole mass spectrometer (QMS, Extrel, QC 150), and eventually recorded by a Daly-type ion counter.[74] The detector is housed within a triply differentially pumped and rotatable chamber that allows the collection of angularly-resolved time-of-flight (TOF) spectra

19762 | *Phys. Chem. Chem. Phys.*, 2022, **24**, 19761–19772

This journal is © the Owner Societies 2022

in the plane defined by both reactant beams. To obtain the information on the reaction dynamics, a forward-convolution method was used to transform the laboratory frame (LAB) data into the center of mass frame (CM),[75,76] which represents an iterative method whereby user-defined CM translational energy $P(E_T)$ and angular $T(\theta)$ flux distributions are varied iteratively until a best fit of the laboratory-frame TOF spectra and angular distributions are achieved. These functions comprise the reactive differential cross-section $I(\theta, u)$, which is taken to be separable into its CM scattering angle θ and CM velocity u components, $I(u, \theta) \sim P(u) \times T(\theta)$. The error ranges of the $P(E_T)$ and $T(\theta)$ functions are determined within the 1σ limits of the corresponding laboratory angular distribution and beam parameters (beam spreads, beam velocities) while maintaining a good fit of the laboratory TOF spectra.

Potential energy profile of reaction $Si(^3P) + O_2(X^3\Sigma_g^-)$. All calculations are carried out with quantum chemistry software MOLPRO.[77] The intermediates, transition states, and products involved in the bimolecular collision of $Si(^3P)$ and $O_2(X^3\Sigma_g^-)$ are characterized at their corresponding ground singlet as well as ground triplet electronic state in order to probe the possible intersystem crossing (ISC). The geometries of the reactants, intermediates, transition states, and products are optimized with complete active space self-consistent field (CASSCF)[78] method with full valence active space (FVAS) and the def2-TZVP[79] basis set. 12 orbitals (e.g., for separated reactants, these orbitals include one 2s and three 2p of each O atom, one 3s and three 3p of Si atom) are included in the active space which hosts 16 valence electrons. The number of harmonic vibrational frequencies is used to verify the identity of an intermediate vs. a transition state. It is interesting to note for **i4**, CASSCF(16, 12) unexpectedly shows three imaginary frequencies with a structure of $D_{\infty h}$ symmetry, while CASSCF with a smaller active space and less electrons (10, 9) converges to the same geometry with zero imaginary frequency. For a more reliable characterization of the potential energy profile of the reaction, the single-point energy of the CASSCF-optimized structures is further refined with the multireference configuration interaction (MRCI)[80] based off the CASSCF wave functions, as MRCI has been proven to be accurate in modeling the potential energy of similar systems[42] with multireference character. The validity of the CASSCF(16, 12)/def2-TZVP and MRCI/def2-TZVP is confirmed by comparing their heat of reaction for both products $(SiO(X^1\Sigma^+) + O(^3P)$ and $SiO(X^1\Sigma^+) + O(^1D))$ with experiments.

Singlet and triplet intersections and spin–orbit coupling. The potential energy surface (PES) of ground singlet and triplet electronic states are scanned in relevant regions of the phase space to investigate possible singlet/triplet intersections. MRCI/def2-TZVP method with state-average (three lowest state, see below) CASSCF wavefunction is employed for this purpose. These regions are identified based on the potential energy profile, in which singlet and triplet surface cross. Specifically,

(1) The geometry space in the vicinity of **i3** (triplet) and **TS14** (singlet), both of which possess C_{2v} symmetry. The geometries are prepared by scanning the (two identical) Si–O bonds from 150 to 190 pm with an increment of 10 pm as well as the O–Si–O bond angle from 72.5 to 120.0° with an increment of 2.5°. A total of 100 geometries are generated, whose potential energy of the lowest singlet state $^1A_1$ and two lowest triplet states $^3B_1$ and $^3B_2$ are calculated.

(2) The geometry space near **i5** (singlet) and **TS2p** (triplet), both of which possess C_s symmetry. To limit the degrees of freedom of the geometry scan, the Si–O bond length is fixed to be 152 pm (identical to the Si–O bond length of **i5**). The O–O bond length is scanned from 150 pm to 240 pm with an increment of 10 angstrom and the Si–O–O bond angle is scanned from 107.5° to 180.0° with an increment of 2.5°. A total of 300 geometries are generated, whose potential energy of the lowest singlet state $(^1A')$ and two lowest triplet states $(^3A'$ and $^3A'')$ are computed.

(3) The geometry space near **i4** (singlet) and **TS3p** (triplet), both of which possess C_s symmetry. To limit the degrees of freedom of the geometry scan, one Si–O bond length is fixed to be 151 pm (identical to the Si–O bond length of **i4**). The other Si–O bond is gradually stretched from 150 to 240 pm with an increment of 10 pm and the O–Si–O bond angle varies between 107.5° to 180.0° with an increment of 2.5°. A total of 300 geometries are generated, whose potential energy of the lowest singlet state $(^1A')$ and two lowest triplet states $(^3A'$ and $^3A'')$ are computed.

The PES is generated from potential energies of discrete geometries with basis spline (B-Spline)[81] function in Python3.8[82] and the seam is defined as where the singlet and triplet PESs cross one other. To estimate the probability of ISC between these two states, spin–orbital coupling (SOC) calculations are also performed at the seam with the Breit–Pauli (BP) spin–orbit operator[80,83] implemented with MOLPRO. The error associated with the SOC calculation from BP is usually smaller than 1 cm^{-1}.[77]

Results & discussion

Crossed molecular beams studies – laboratory frame

Reactive scattering signal for the bimolecular reaction of the atomic silicon (Si; ^3P) with molecular oxygen $(^{18}O_2; X^3\Sigma_g^-)$ was only observed at mass-to-charge ratios (m/z) of 46 $(^{28}Si^{18}O^+)$. No adduct at m/z = 64 $(^{28}Si^{18}O_2)$ was detectable. The reactive scattering signal monitored at m/z 46 $(^{28}Si^{18}O^+)$ alone suggests an open reaction channel leading to silicon monoxide $(^{28}Si^{18}O;$ 46 amu; hereafter: SiO) along with an oxygen atom (O; 18 amu), i.e., the presence of a silicon atom versus atomic oxygen exchange channel (reaction (1a) and (1b)). The corresponding TOF spectra and the laboratory angular distribution (LAD) were collected at m/z = 46 (Fig. 1). The LAD is rather broad and spans the complete range of the detector spread from at least 9.25° to 66.25°.

Crossed molecular beams studies – center-of-mass frame

The laboratory data alone offer explicit evidence on the gas phase formation of silicon monoxide (SiO, $X^1\Sigma^+$) along with atomic oxygen under single collision conditions. However, the prime directive of our studies is not only to unravel the nascent reaction product formed, but also to reveal the underlying
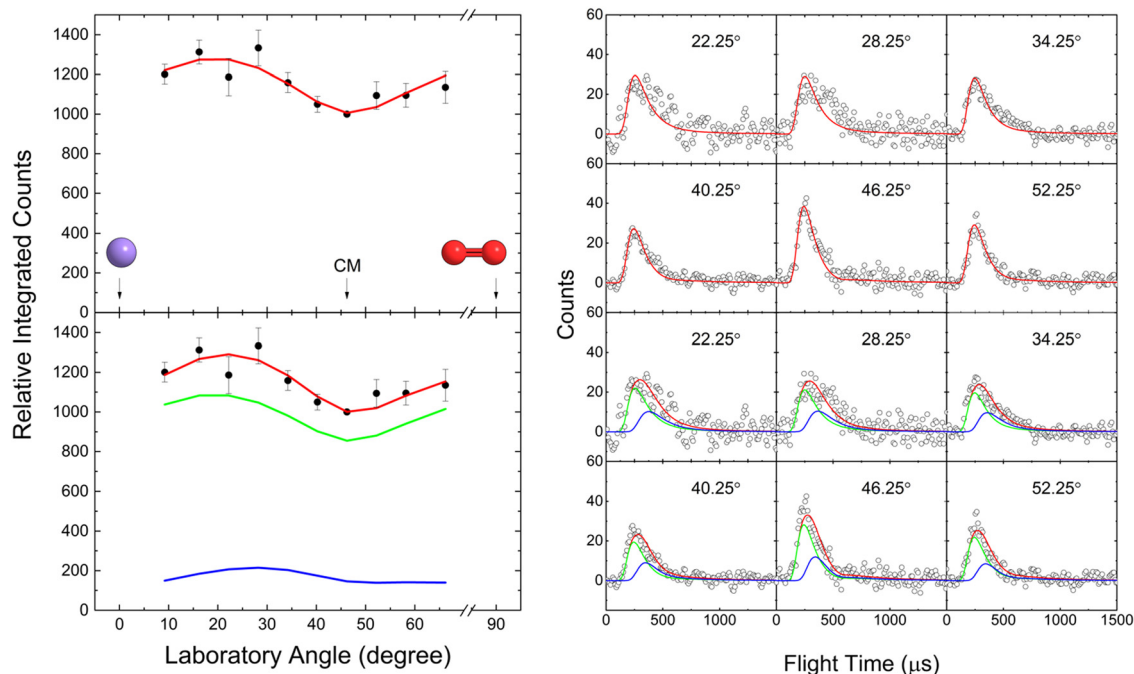
Fig. 1 Laboratory angular distribution (left) and time-of-flight (TOF) spectra (right) recorded at $m/z = 46$ for the reaction of the silicon atom (Si; ^3P) with molecular oxygen ($^{18}O_2$; $X^3\Sigma_g^-$). The data were fit with a single channel (top), and with two channels (bottom): (i) $^{28}Si(^3P$; 28 amu) + $^{18}O_2(X^3\Sigma_g^-$; 36 amu) → $^{28}Si^{18}O(X^1\Sigma^+$; 46 amu) + $^{18}O(^3P$; 18 amu) (green), (ii) $^{28}Si(^3P$; 28 amu) + $^{18}O_2(X^3\Sigma_g^-$; 36 amu) → $^{28}Si^{18}O(X^1\Sigma^+$; 46 amu) + $^{18}O(^1D$; 18 amu) (blue). CM represents the center-of-mass angle, and 0° and 90° define the directions of the silicon atom and molecular oxygen beams, respectively. The black circles depict the experimental data, colored lines the fits (red corresponding to the total fit), and error bars the 1σ standard deviation.

reaction mechanism(s) along with the potential involvement of excited state surfaces, ISC, and non-adiabatic reaction dynamics. This requires a transformation of the laboratory data (TOF, LAD) into the center-of-mass reference frame resulting in the center-of-mass translational energy $P(E_T)$ and angular $T(\theta)$ flux distribution (Fig. 2).
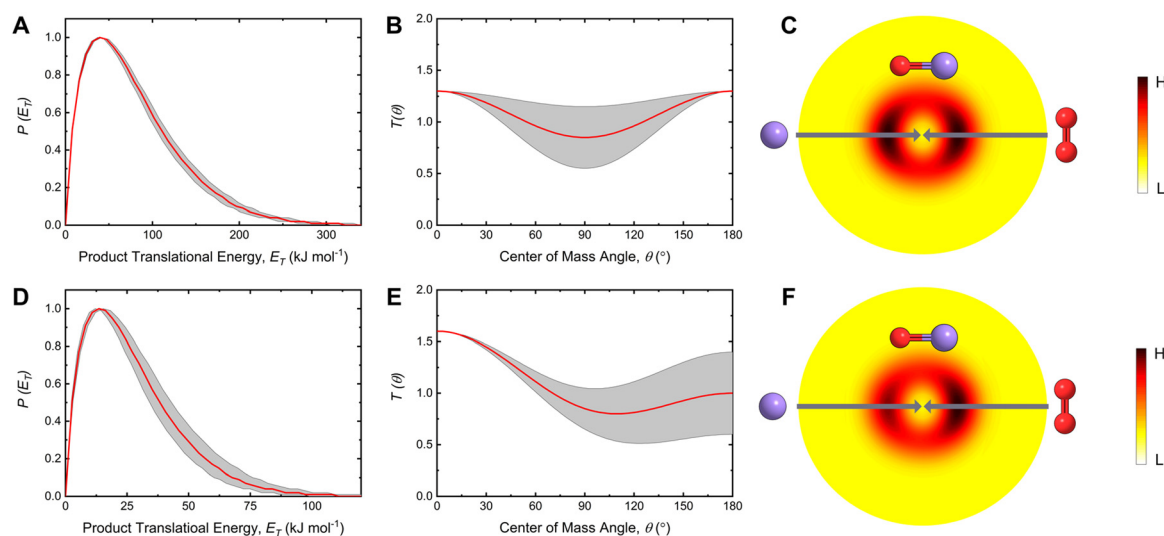

Fig. 2 CM translational energy flux distribution (A and D), CM angular flux distribution (B and E), and the top view of the flux contour map (C and F) for the reaction of ground state atomic silicon (^{28}Si; ^3P) and molecular oxygen ($^{18}O_2$; $X^3\Sigma_g^-$). (A), (B), and (C) are corresponding to the reaction of $^{28}Si(^3P$; 28 amu) + $^{18}O_2(X^3\Sigma_g^-$; 36 amu) → $^{28}Si^{18}O(X^1\Sigma^+$; 46 amu) + $^{18}O(^3P$; 18 amu). (D), (E), and (F) are responsible for the reaction of $^{28}Si(^3P$; 28 amu) + $^{18}O_2(X^3\Sigma_g^-$; 36 amu) → $^{28}Si^{18}O(X^1\Sigma^+$; 46 amu) + $^{18}O(^1D$; 18 amu). Shaded areas indicate the acceptable upper and lower error limits, while the red solid lines define the best fits. The flux contour map represents the flux intensity of the reactively scattered heavy products as a function of the CM scattering angle (θ) and product velocity (u). The color bar manifests the flux gradient from high (H) intensity to low (L) intensity. Colors of the atoms: silicon, purple; oxygen, red.

Single channel fit

Within our error limits, the TOFs and LAD at $m/z = 46$ (Fig. 1) could be replicated through a single channel fit corresponding to the reaction $^{28}Si(^3P$; 28 amu) + $^{18}O_2(X^3\Sigma_g^-$; 36 amu) → $^{28}Si^{18}O(X^1\Sigma^+$; 46 amu) + $^{18}O(^3P$; 18 amu) (reaction (1a)) (Fig. 1 (top)). The resulting CM translational energy distribution $P(E_T)$ terminates at 322 ± 17 kJ mol^{-1} (Fig. 2A); this energy represents the maximum translational energy (E_{max}) release for those species formed without rovibrational or electronic excitation. Considering the principle of energy conservation, the maximum translational energy (E_{max}), collision energy (E_C), and the reaction energy ($\Delta_r G$) are connected *via* $E_{max} = E_C - \Delta_r G$ for those products born without internal excitation. Consequently, reaction (1a) is exoergic by 310 ± 17 kJ mol^{-1}. Further, the $P(E_T)$ distribution peaks at 39 ± 2 kJ mol^{-1} suggesting a tight exit transition state yielding the silicon monoxide molecule plus atomic oxygen from SiO$_2$ reaction intermediate(s).[84] The average translational energy of the products was derived to be 80 ± 4 kJ mol^{-1}; this means that only $25 \pm 1\%$ of the maximum available energy is channeled into the translational degrees of freedom of the products. Additional information on the reaction dynamics can be collected by inspecting the center-of-mass angular flux distribution $T(\theta)$ (Fig. 2B). First, the $T(\theta)$ is forward–backward symmetric and depicts flux over the complete angular range from $0°$ to $180°$; this proposes indirect scattering dynamics *via* complex formation and hence the existence of bound triatomic intermediate(s). The distribution minimum at $90°$ proposes geometrical limitations and an emission of the oxygen atom nearly perpendicularly to the total angular momentum vector within the rotational plane of the fragmenting complex(es).[85]

Two channels fit

Each TOF spectrum (Fig. 1 (right)) is rather broad and spread over up to 500 µs. All TOFs reveal a fast component at 200–300 µs. However, at lower laboratory angles especially at $22.25°$ and $28.25°$, a slower component is also evident at about 470 µs. These findings indicate that more than one reaction channel might be involved (Table S2, ESI†). The fast peak of the TOFs could be replicated exceptionally well with the reaction $^{28}Si(^3P$; 28 amu) + $^{18}O_2(X^3\Sigma_g^-$; 36 amu) → $^{28}Si^{18}O(X^1\Sigma^+$; 46 amu) + $^{18}O(^3P$; 18 amu) (reaction (1a)); the slower peak can only be accounted for by introducing a second channel $^{28}Si(^3P$; 28 amu) + $^{18}O_2(X^3\Sigma_g^-$; 36 amu) → $^{28}Si^{18}O(X^1\Sigma^+$; 46 amu) + $^{18}O(^1D$; 18 amu) (reaction (1b)). Therefore, we evaluated objectively a two-channel incorporating reactions (1a) and (1b) (Fig. 1 (bottom)). This two-channel fit could also reproduce the laboratory data with branching ratios of $85 \pm 5\%$ and $15 \pm 2\%$ for reaction (1a) and (1b), respectively. This finding suggests that to a minor amount, up to $15 \pm 2\%$ of the reaction products might lead to the production of electronically excited oxygen atoms ($^{18}O(^1D)$). It should be noted that a one-channel fit involving only reaction (1b) could not fit the laboratory data with TOF spectra being too slow and the LAD distribution too narrow (Fig. S1, ESI†). The corresponding center-of-mass functions of channel (1b) are displayed in Fig. 2D and E revealing a

maximum translational energy (E_{max}) of 111 ± 13 kJ mol^{-1} and hence a reaction energy of -99 ± 13 kJ mol^{-1}. The difference in reaction energies of reactions (1a) and (1b) of 211 ± 30 kJ mol^{-1} matches nicely the triplet–singlet gap of atomic oxygen of 190 kJ mol^{-1}. Further, the $P(E_T)$ distribution maximum located at 14 ± 2 kJ mol^{-1} suggests a rather loose exit transition state from the decomposing SiO$_2$ intermediate(s) to the final products. This loose transition state for reaction (1b) is rather distinct from the rather tight exit transition state for reaction (1a). The average translational energy for channel (1b) of the products was deduced to be 28 ± 3 kJ mol^{-1} indicating that $25 \pm 3\%$ of the available energy is disposed into the translational degrees of freedom of the products. Finally, the $T(\theta)$ portrays a forward scattering with an intensity ratio $I(0°)/I(180°)$ of about $(1.9 \pm 0.8):1.0$. These data suggest that the existence of at least one pathway involves an osculating complex, where a complex formation takes place, but the lifetime of the complex is too low to allow multiple rotations to complete.[85,86]

Triplet and singlet potential energy surface (PES)

The intimate chemical dynamics of the reaction of atomic silicon (Si; ^3P) with molecular oxygen (O$_2$; $X^3\Sigma_g^-$) can be unraveled by merging the laboratory data with electronic structure calculations conducted at the MRCI/def2-TZVP//CASSCF(16, 12)/def2-TZVP level of theory (Fig. 3).[78–80] We note that reaction pathways that are energetically inaccessible under our experimental conditions are not included; for example, the products of the first excited triplet state of silicon monoxide (SiO($a^3\Sigma^+$) + O(^3P); SiO($a^3\Sigma^+$) + O(^1D)) are 100 kJ mol^{-1} and 295 kJ mol^{-1} above the total energy of the separated reactants, respectively, and hence energetically not accessible at the collision energy of 11.9 kJ mol^{-1}. The electronic structure calculations reveal the existence of two atomic oxygen loss channels: silicon monoxide (SiO; $X^1\Sigma^+$) plus ground state atomic oxygen (**p1**, O(^3P), $\Delta_r G = -303 \pm 5$ kJ mol^{-1}; reaction (1a)) and electronically excited singlet oxygen (**p2**, O(^1D), $\Delta_r G = -107 \pm 5$ kJ mol^{-1}; reaction (1b)) at the MRCI/def2-TZVP//CASSCF/def2-TZVP level. The computed reaction energy of **p1** and **p2** agree exceptionally well with the reaction exoergicity of 301 ± 8 kJ mol^{-1} and 112 ± 8 kJ mol^{-1} derived from the standard enthalpies of formations extracted from NIST.[87–89] As demonstrated through the aforementioned two-channel fit, a comparison of the computed reaction energies (**p1**, $\Delta_r G = -303 \pm 5$ kJ mol^{-1}; **p2**, $\Delta_r G = -107 \pm 5$ kJ mol^{-1}) with the experimentally derived value from the crossed beam study ($\Delta_r G = -310 \pm 17$ kJ mol^{-1}) suggests that at least silicon monoxide (SiO; $X^1\Sigma^+$) plus ground state atomic oxygen (O(^3P)) (**p1**) is formed. The channel to **p2** might be masked in the low-energy part of the center-of-mass translational energy distribution with a fraction of $15 \pm 2\%$. We note that it is necessary to employ high-level multireference method such as MRCI, as the reaction energy computed from lower-level method such as CASSCF/def2-TZVP is not accurate, yielding -384 kJ mol^{-1} and -174 kJ mol^{-1} for reaction (1a) and (1b), respectively. Similarly, single reference methods, even at the couple cluster level with complete basis set such as CCSD(T)/CBS,[90,91] do not accurately represent reaction energy of the singlet channel, for example, **p2** is predicted to be -90 kJ mol^{-1} for CBS
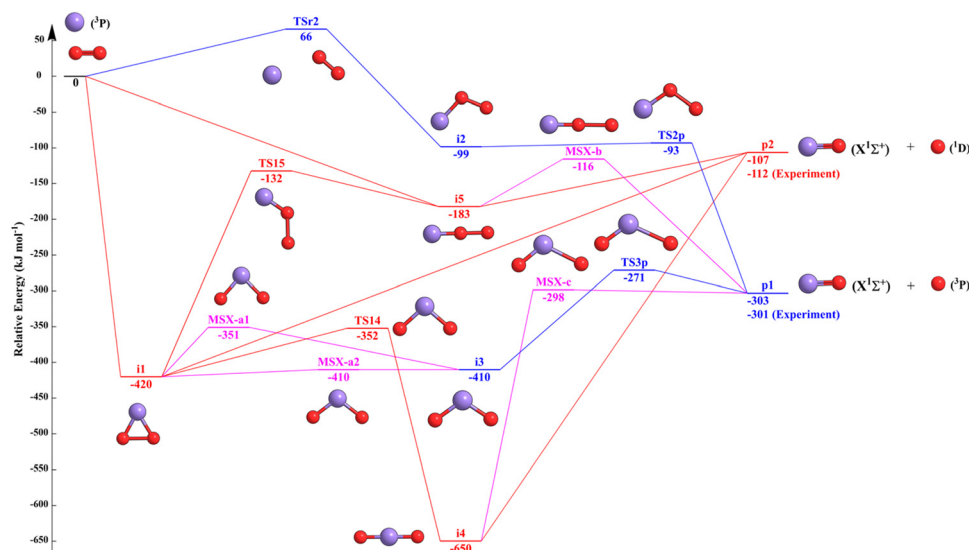
Fig. 3 Ground state singlet (red) and excited state triplet (blue) potential energy surfaces (PES) of the bimolecular reaction of atomic silicon (Si(^{3}P)) with molecular oxygen (O$_2$(X$^3\Sigma_g^-$)). The minima on the seam-of-crossings (MSX) pathways are indicated in pink. The relative energies are given in kJ mol^{-1} calculated with MRCI/def2-TZVP//CASSCF/def2-TZVP level of theory (CASSCF/def2-TZVP zero-point energy included). TS = transition states; r = reactants; p = products.

extrapolated from triple-zeta, quadruple-zeta, and quintuple-zeta basis sets (Table S3, ESI†). Therefore, MRCI/def2-TZVP//CASSCF/ def2-TZVP is employed for characterizing the potential energy surface depicted in Fig. 3.

To sum up, our data reveal the dominant formation of silicon monoxide (SiO; X$^1\Sigma^+$) along with ground state atomic oxygen (O(^{3}P)) under single collision conditions in the gas phase with smaller fractions of the reactive scattering signal possibly originating from the singlet surface (O(^{1}D)). But what is(are) the dominating reaction mechanisms? Accounting for the ^{3}P$_j$ and $^3\Sigma_g^-$ electronic ground states of the silicon atom and of molecular oxygen, respectively, together with the X$^1\Sigma^+$ and ^{1}D/^{3}P electronic states of the silicon monoxide and atomic oxygen, both the triplet and singlet surfaces have to be explored. As shown in Fig. 3, our computations located three singlet (**i1, i4, i5**) and two triplet (**i2, i3**) SiO$_2$ intermediates. The reaction can be initiated *via* a barrierless addition of ground-state silicon (Si, ^{3}P) to the one of the oxygen atoms of molecular oxygen molecule forming a linear singlet (SiOO, **i5**, $C_{\infty v}$, X$^1\Sigma^+$) collision complex. However, a similar addition on the triplet surface has to overcome a barrier (SiOO, **TSr2**, C_s, X^{3}A″) of 66 kJ mol^{-1} before forming a bent triplet (SiOO, **i2**, C_s, X^{3}A″) collision complex, thus this entrance channel is not accessible under our experimental condition at a collision energy of only 11.9 kJ mol^{-1}. It is important to note that there was no entrance barrier reported in previous work[43] with a smaller basis set, but we found **TSr2** by saddle point optimization without any geometrical constraint. **TSr2** has been confirmed by vibrational frequency and intrinsic reaction coordinate (IRC) calculations (Fig. S2, ESI†).[92–94] Nonetheless, if **i2** could be formed (*e.g.*, from ISC), it can emit an oxygen atom from the terminal position after overcoming a loose transition state (**TS2p**) to form silicon monoxide (SiO, $C_{\infty v}$, X$^1\Sigma^+$) along with ground state

atomic oxygen (**p1**, O(^{3}P)). The same products can be formed from another triplet intermediate, **i3** (OSiO, C_{2v}, X^{3}B$_2$), which can undergo unimolecular decomposition *via* transition state **TS3p**. On the singlet surface, intermediate **i1** (OSiO, C_{2v}, X^{1}A$_1$) can be formed barrierlessly in one-step from the reactants in nearly zero impact parameter collisions; this intermediate then ring opens to silicon dioxide **i4** (OSiO, $D_{\infty h}$, X$^1\Sigma_g^+$) *via* a transition state lying 68 kJ mol^{-1} above **i1** following C_{2v} symmetry. Linear singlet silicon dioxide **i4** represents the global minimum of the potential energy surface. Intermediate **i1** (OSiO, C_{2v}, ^{1}A$_1$) could also isomerize to **i5** (SiOO, $C_{\infty v}$, X$^1\Sigma^+$), which could also be formed barrierlessly in one-step from the collision between reactants. The product silicon monoxide (SiO; X$^1\Sigma^+$) along with electronically excited singlet oxygen (**p2**, O(^{1}D)) can be formed *via* emission of an atomic oxygen in **i1, i4**, and **i5**.

Intersystem crossing

To gauge the role of intersystem crossing (ISC) between the triplet and singlet surfaces, the computations were expanded to identify minima on the seam-of-crossings (MSX). ISC is likely observable in the geometrical spaces where their singlet and triplet electronic states are close in energy and have strong spin–orbit coupling (SOC).[95] To identify potential geometrical regions that are the most relevant to ISC, the vertical excitation energies of the intermediates and transition states identified in Fig. 3 are computed (Table S4, ESI†). According to Table S4 (ESI†), three regions most relevant to the ISC are identified, whose corresponding PESs and SOCs are scanned and depicted in Fig. 4. First, the singlet energy **i1** is lower than the energy of its triplet state by 246 kJ mol^{-1}. The singlet *versus* triplet energy is reversed for the transition state (**TS14**) connecting **i1** and **i4** on the singlet surface, whose singlet energy is 33 kJ mol^{-1}

higher than the triplet. Interestingly, a geometrically alike structure, **i3**, is optimized on the triplet surface, where its singlet energy is 49 kJ mol^{-1} lower. All this evidence suggests that the singlet and the triplet surfaces cross one another when **i1** ring opens and silicon formally inserts into the O–O bond. Since all three structures (**i1**, **TS14**, and **i3**) possess C_{2v} symmetry, the C_{2v} geometries are employed for the energy scan to reduce the number of calculations. As shown in Fig. 4a, two seams primarily defined by the O–Si–O angle are identified. The first seam holds an O–Si–O angle of close to 80°, indicating the ISC could take place in the process of **i1** ($\angle$(O–Si–O) = 58°) crossing the barrier **TS14** ($\angle$(O–Si–O) = 97°). The second seam possesses an O–Si–O angle between 105 and 120°, indicating that the ISC could take place after the transition state **TS14** before forming the linear intermediate **i4** ($\angle$(O–Si–O) = 180°). Minimum energy crossing points (MSX) optimization without any geometry constraint were also performed at the CASSCF/def2-TZVP level using a Lagrange multiplier to impose a constraint of equal energy upon the two states.[96] The geometrical parameters of **MSX-a1** (Table S5, ESI†) are close **TS14** with a 10° smaller O–Si–O angle, while the geometrical parameters of **MSX-a2** are close to **i3** with an O–Si–O angle smaller by 6°.

In order to assess the probability of ISC, the SOC is scanned with the orbitals calculated with MRCI/def2-TZVP and depicted in Fig. 4b. The SOC values are 0.02, 46.51, 24.96, and 43.45 cm^{-1} for **TS14**, **i3**, **MSX-a1**, and **MSX-a2**, respectively, indicating that once **i1** forms on the singlet surface, it could cross to the triplet surface before or after crossing **TS14** to form **i3** or remains on the singlet surface to form **i4**.

Second, the singlet energy of **i5** ($\angle$(Si–O–O) = 180°) is 218 kJ mol^{-1} lower than its triplet energy. This energy difference becomes smaller as the Si–O–O angle bends, *e.g.*, only 50 kJ mol^{-1} for the intermediate on the triplet surface, **i2** (($\angle$(Si–O–O) = 110°). Considering that the singlet product is higher in energy than its triplet counterpart, which geometrically is a result of stretching the O–O distance in structures like **i5** and **i2**, ISC could take place. As shown in Fig. 4c, the energy difference between the singlet and the triplet surfaces are very sensitive to the O–O distance. One seam is identified between these two surfaces with a Si–O distance of 170 pm. The SOC of this geometrical space is computed (Fig. 4d) and is rather consistent (60–61 cm^{-1}) along the seam. **MSX-b** is identified and its geometry is visualized in Table S5 (ESI†). Intermediate **i5** could encounter the seam as the O–O bond length increases,
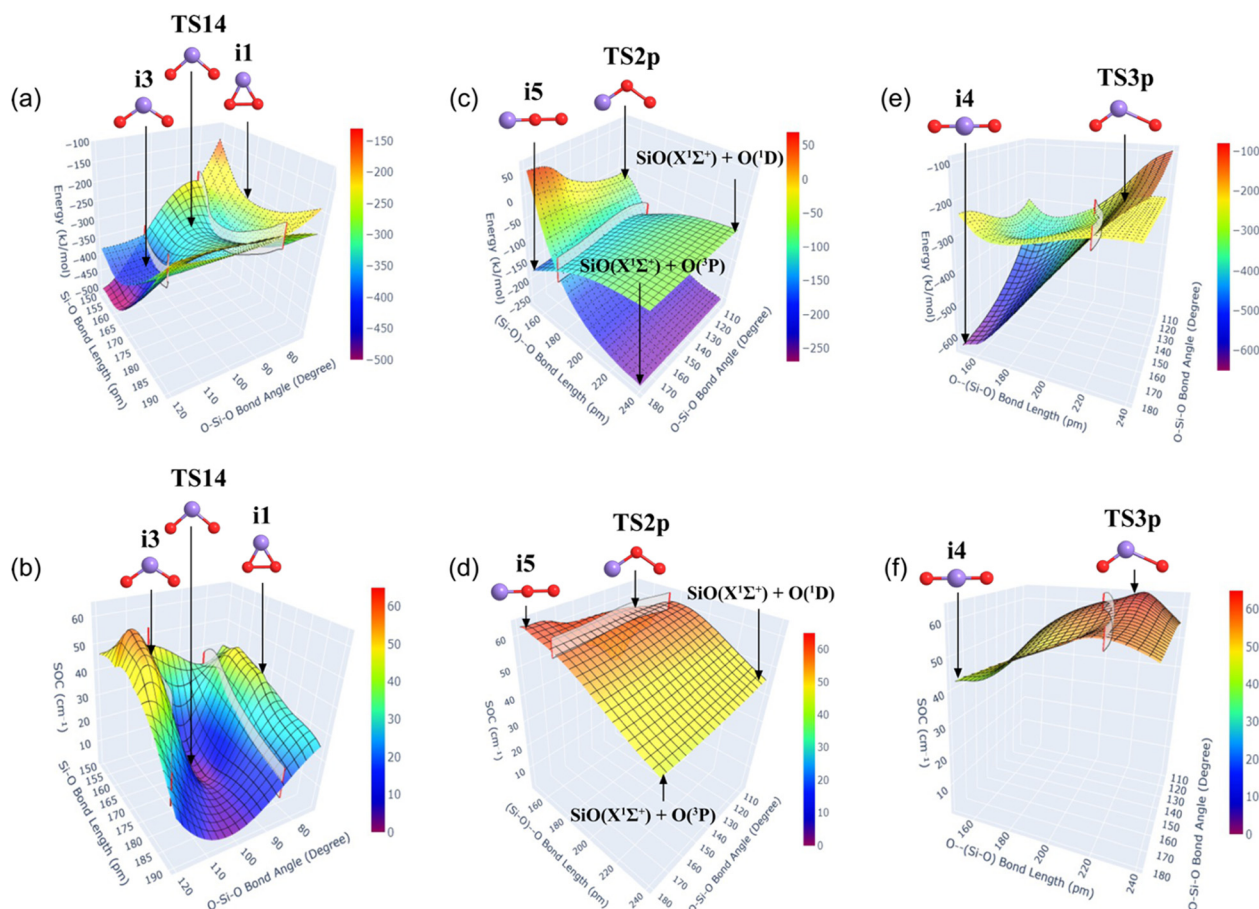
Fig. 4 Singlet and triplet intersections (top column) and spin–orbit coupling (SOC, bottom column). The energies (kJ mol^{-1}) and SOC (cm^{-1}) are scanned using the MRCI/def2-TZVP method. The singlet and triplet PESs are shown in a solid and dashed grid, respectively. The seam where the singlet and triplet surface cross is marked with a transparent ribbon. TS: transition state; r = reactants; p = products.

This journal is © the Owner Societies 2022

Phys. Chem. Chem. Phys., 2022, **24**, 19761–19772 | **19767**

transits to the triplet surface, and forms the triplet products silicon monoxide (SiO, $C_{\infty v}$, $X^1\Sigma^+$) along with ground state atomic oxygen (**p1**, $O(^3P)$) with the seam only residing about 67 kJ mol^{-1} above **i5**, as compared to 76 kJ mol^{-1} to form silicon monoxide (SiO, $C_{\infty v}$, $X^1\Sigma^+$) along with excited state atomic oxygen (**p2**, $O(^1D)$).

Third, ISC could take place in an alternative exit channel. This can be seen by considering the stretch of the Si–O distance in **i4** on the singlet surface and of **i3** on the triplet surface, leading to the products with the triplet surface being lower in energy than the singlet surface (Fig. 3). Note for both **i4** and **i3**, their singlet energy is lower than the triplet energy by 499 and 49 kJ mol^{-1}, respectively. Therefore, both the singlet and triplet surfaces are scanned for the relevant geometrical space (Fig. 4e). Similar to the previous case, the energy difference between these two surfaces is sensitive to the Si–O distance and the O–Si–O angle as the seam is found to start at 200 pm and 110° and ends at 200 pm and 180°. **MSX-c** is identified and its geometry is presented in Table S5. The seam possesses a relative stable SOC of 59–60 cm^{-1} (Fig. 4f). The position of the seam indicates that the oscillation of **i4** on the singlet surface could lead to ISC to the triplet surface and eventually dissociate to silicon monoxide (SiO, $C_{\infty v}$, $X^1\Sigma^+$) along with ground state triplet atomic oxygen (**p1**, $O(^3P)$). This process is much more favorable in energy as the seam is about 352 kJ mol^{-1} above **i4**, as compared to 543 kJ mol^{-1} for the singlet products silicon monoxide (SiO, $C_{\infty v}$, $X^1\Sigma^+$) plus excited state atomic oxygen (**p2**, $O(^1D)$).

Overall, although both the singlet and triplet channels are energetically allowed for the bimolecular reaction of ground state silicon atoms with molecular oxygen, under the experimental conditions, the triplet channel to silicon monoxide (SiO, $C_{\infty v}$, $X^1\Sigma^+$) along with ground state triplet atomic oxygen (**p1**, $O(^3P)$) is predicted to be the dominant product following the pathway **i1 → MSX-a1/2 → i3 → TS3p → p1** and **i5 → MSX-b → p1**. The favored mechanism to the singlet products follows **i5 → p2**.

Reaction pathways

A combination of the experimental data with the computational results assists in narrowing down the proposed pathways. The distribution maximum of the center-of-mass translational energy distribution of about 40 kJ mol^{-1} proposes a tight exit transition state leading to silicon monoxide (SiO; $X^1\Sigma^+$) plus ground state atomic oxygen (**p1**, $O(^3P)$) – the dominant exit channel with fractions of at least 85 ± 5%. The exit barrier of the unimolecular decomposition of **i4** of only 5 kJ mol^{-1} would result in a center-of-mass translational distribution peaking close to zero translational energy; therefore, this pathway can be excluded. The unimolecular decomposition of intermediates **i3**, and **i5** *via* an exit transition state located 32 and 187 kJ mol^{-1} above the energy of the separated products can account for the experimentally observed 'off-zero' peaking of the center-of-mass translational energy distribution leading to the triplet products to silicon monoxide (SiO; $X^1\Sigma^+$) plus ground state atomic oxygen (**p1**, $O(^3P)$). However, compared with the experimental determined

peaking value of 40 kJ mol^{-1} of the center-of-mass translational energy distribution, the favored pathway would be **i3 → TS3p → p1** (32 kJ mol^{-1}), other than **i5 → MSX-b → p1** (187 kJ mol^{-1}). The pathway **i5 → MSX-b → p1** can be ruled out at the present stage. Therefore, the reaction path **i1 → MSX-a1/2 → i3 → TS3p → p1** correlate nicely with the experimental results, which was also predicted from the computational investigation of the surfaces. Further, the center-of-mass angular distribution features a minimum at 90°; this finding documents a decomposition of the SiO_2 intermediate in which the oxygen atom is eliminated nearly perpendicularly to the total angular momentum vector within the rotation plane of the fragmenting complex. The computed geometry of **TS3p** to **p1** plus ground state atomic oxygen can explain the in-plane scattering dynamics with atomic oxygen emitted within the plane of the decomposing complex.

Astrochemical implication

Our study explicitly identifies silicon monoxide (SiO; $X^1\Sigma^+$) – the fundamental molecular building block to a low temperature population of interstellar silicates formed in cold molecular clouds. The largest fractional abundances of silicon monoxide (SiO; $X^1\Sigma^+$) in star forming regions of up to a few 10^{-6} with respect to molecular hydrogen and in the circumstellar envelopes (CSEs) around Asymptotic Giant Branch (AGB) stars[97] contrasts extremely low abundances in cold molecular clouds like TMC-1 and L183 of a few 10^{-12}. Here, upon formation, silicon monoxide (SiO; $X^1\Sigma^+$) can rapidly deplete on interstellar grains thus facilitating molecular mass growth of interstellar grains even at temperatures as low as 10 K. Indeed, silicate grains may form in the interstellar medium at cryogenic temperatures through the oligomerization of silicon monoxide (SiO; $X^1\Sigma^+$).[30–36] The explicit identification of silicon monoxide (SiO; $X^1\Sigma^+$) in the present work therefore removes one of the key uncertainties in astrochemical models. In shocked regions, the ice can be removed to (partially) recycle silicon monoxide (SiO; $X^1\Sigma^+$) back into the gas phase. Where shocks are strong enough to destroy the grain core as well, then the silicon monoxide (SiO; $X^1\Sigma^+$) gas phase abundance can be quite large up to 10% of the cosmic silicon. Note that alternative gas-phase pathways to silicon monoxide exist, such as the experimentally unexplored reaction of ground state silicon atoms with the hydroxyl radical (OH), which may also lead to silicon monoxide.[98] However, in the cold gas, fractional abundances of the hydroxyl radical (OH) are a factor of 10^2–10^3 lower than for molecular oxygen (O_2) with Herschel observations proposing fractional abundances of up to 10^{-4}.[99–101] This abundance agrees well with a molecular oxygen to water ratio of 0.038 recently detected in comet 67P/Churyumov–Gerasimenko[102] with Taquet *et al.* arguing that the high abundance of oxygen present in 67P is of interstellar origin.[103]

Conclusions

Combining crossed molecular beams experiments with electronic structure calculations, this work affords compelling evidence on the dominant formation of silicon monoxide (SiO; $X^1\Sigma^+$) along

19768 | *Phys. Chem. Chem. Phys.*, 2022, **24**, 19761–19772

This journal is © the Owner Societies 2022

with ground state atomic oxygen (O(^{3}P)) *via* non-adiabatic reaction dynamics through the bimolecular neutral – neutral reaction of ground state silicon atoms with molecular oxygen under gas-phase single-collision conditions prevailing in cold molecular clouds such as the Taurus Molecular Cloud-1. The dominating reaction mechanism commences on the singlet manifold and involves the barrierless addition of atomic silicon to the oxygen molecule forming cyclic silicon dioxide intermediate (**i1**), which then isomerizes while experiencing ISC to the triplet surface *via* ring opening to an acyclic triplet silicon dioxide (**i3**); the latter undergoes unimolecular decomposition *via* a tight exit transition state with the oxygen atom emitted within the rotational plane of the decomposing complex yielding silicon monoxide (SiO; X$^1\Sigma^+$) along with ground state atomic oxygen (O(^{3}P)). With only $25 \pm 1\%$ of the total available energy released into the translational degrees of freedom, the internal energy may populate up to 22 vibrational levels in silicon monoxide (SiO; X$^1\Sigma^+$) at most. First, it is important to address the barrierless character of the entrance channel on the singlet surface. The addition of the silicon atom to the π electronic system of molecular oxygen has no barrier since it involves an association of two reactants, which each have both two unpaired electrons thus creating two new silicon-oxygen bonds in the C_{2v} symmetric singlet silicon dioxide. This entrance-barrierless feature of this reaction is also supported through kinetics studies by Martin *et al.*, Husain *et al.*, and Le Picard *et al.* down to temperatures as low as 15 K.[38–41] The absence of any barrier represents a crucial prerequisite for the reaction of atomic silicon with molecular oxygen to form silicon monoxide (SiO; X$^1\Sigma^+$) in cold molecular clouds with typical temperatures as low as 10 K. Second, the dissociation of triplet **i3** (OSiO, C_{2v}, X^{3}B$_2$) to silicon monoxide (SiO; X$^1\Sigma^+$) plus ground state atomic oxygen (O(^{3}P)) can be compared to the unimolecular decomposition of the isovalent carbon dioxide (CO$_2$) system. Previous studies of these systems revealed that the dominant photodissociation pathways of carbon dioxide following 157 nm are the O(^{3}P) and O(^{1}D) channels with a branching ratio of the spin-forbidden O(^{3}P) channel ranging from 6 to 12%.[104–107] However, whereas the nonadiabatic dynamics in the triplet exit channel for carbon dioxide (CO$_2$) represent only a minor channel, the heavy atom effect may promote ISC as a predominant, if not an exclusive channel for the dynamics of the ground state silicon – molecular oxygen system; recall that the inclusion of heavy atoms like silicon in the molecular structure enhances the spin–orbit coupling between singlet and triplet states. Third, at a collision energy of 11.9 ± 3.0 kJ mol^{-1}, our findings propose dominant indirect scattering dynamics leading to silicon monoxide (SiO; X$^1\Sigma^+$) plus ground state atomic oxygen (O(^{3}P)). This contradicts previous quasiclassical trajectory (QCT) studies, which propose prevailing backward scattering (70%) and complex forming (30%) dynamics.[44,108] This apparent mismatch can be rationalized by realizing that the QCT studies were conducted on the analytical ground ^{1}A$'$ surface and did not consider conical intersections and hence the ISC is absent.

Overall, the bimolecular elementary reaction of ground state silicon atoms with molecular oxygen provides a single collision event forming silicon monoxide (SiO; X$^1\Sigma^+$) along with ground state atomic oxygen (O(^{3}P)) through non-adiabatic reaction dynamics. In the cold interstellar medium, silicon monoxide (SiO; X$^1\Sigma^+$) may either deplete on interstellar grains thus leading to silicon oxide clusters in barrierless reactions,[30] or alternatively, if sufficient hydroxyl radicals are available for reaction, silicon monoxide (SiO; X$^1\Sigma^+$) could react barrierlessly with the hydroxyl radical (OH) forming silicon dioxide (SiO$_2$; X$^1\Sigma_g^+$) plus atomic hydrogen in an exoergic reaction.[109] The capability of barrierless, exoergic reactions between silicon monoxide and silicon dioxide enhanced the critical role of silicon monoxide in the formation of larger silicon oxides (Si$_2$O$_5$, Si$_3$O$_5$) suggesting that the silicon – molecular oxygen system may play a central role in initiating the complex set of elementary reactions leading ultimately to a population of silicates in the low temperature interstellar medium. Since interstellar dust such as silicate grains (have) play(ed) a fundamental role in the formation of Solar Systems including our own and ice-coated grains provide essential molecular factories for an abiotic formation of biorelevant molecules like sugars and amino acids,[6–9] the untangling of the reaction mechanisms from the fundamental, microscopic point of view is essential how we reflect on our Origins.

Conflicts of interest

The authors declare no competing interest.

Acknowledgements

References

1 C. F. Mabery, *J. Franklin Inst.*, 1886, **122**, 271–274.

2 L. M. Ziurys, *Proc. Natl. Acad. Sci. U. S. A.*, 2006, **103**, 12274–12279.

3 T. P. M. Goumans and S. T. Bromley, *Mon. Not. R. Astron. Soc.*, 2012, **420**, 3344–3349.

4 T. Henning, *Annu. Rev. Astron. Astrophys.*, 2010, **48**, 21–46.

5 A. P. Jones and J. A. Nuth III, *Astron. Astrophys.*, 2011, **530**, A44.

6 R. Larralde, M. P. Robertson and S. L. Miller, *Proc. Natl. Acad. Sci. U. S. A.*, 1995, **92**, 8158–8160.

7 C. Meinert, I. Myrgorodska, P. De Marcellus, T. Buhse, L. Nahon, S. V. Hoffmann, L. L. S. d'Hendecourt and U. J. Meierhenrich, *Science*, 2016, **352**, 208–212.

8 G. M. Muñoz Caro, U. J. Meierhenrich, W. A. Schutte, B. Barbier, A. Arcones Segovia, H. Rosenbauer, W. H.-P. Thiemann, A. Brack and J. M. Greenberg, *Nature*, 2002, **416**, 403–406.

9 A. K. Cobb and R. E. Pudritz, *Astrophys. J.*, 2014, **783**, 140.

This journal is © the Owner Societies 2022

Phys. Chem. Chem. Phys., 2022, **24**, 19761–19772 | **19769**

10 V. Wakelam, I. W. M. Smith, E. Herbst, J. Troe, W. Geppert, H. Linnartz, K. Öberg, E. Roueff, M. Agúndez, P. Pernot, H. M. Cuppen, J. C. Loison and D. Talbi, *Space Sci. Rev.*, 2010, **156**, 13–72.

11 N. G. Holm, C. Oze, O. Mousis, J. H. Waite and A. Guilbert-Lepoutre, *Astrobiology*, 2015, **15**, 587–600.

12 G. Vidali, J. Roser, G. Manicó, V. Pirronello, H. B. Perets and O. Biham, *J. Phys.: Conf. Ser.*, 2005, **6**, 36.

13 P. Ehrenfreund and S. B. Charnley, *Annu. Rev. Astron. Astrophys.*, 2000, **38**, 427–483.

14 H.-P. Gail and E. Sedlmayr, *Astron. Astrophys.*, 1999, **347**, 594–616.

15 A. C. Reber, P. A. Clayborne, J. U. Reveles, S. N. Khanna, A. W. Castleman and A. Ali, *Nano Lett.*, 2006, **6**, 1190–1195.

16 A. C. Reber, S. Paranthaman, P. A. Clayborne, S. N. Khanna and A. W. Castleman Jr, *ACS Nano*, 2008, **2**, 1729–1737.

17 D. Gobrecht, I. Cherchneff, A. Sarangi, J. M. C. Plane and S. T. Bromley, *Astron. Astrophys.*, 2016, **585**, A6.

18 H.-P. Gail, S. Wetzel, A. Pucci and A. Tamanai, *Astron. Astrophys.*, 2013, **555**, A119.

19 H.-P. Gail, M. Scholz and A. Pucci, *Astron. Astrophys.*, 2016, **591**, A17.

20 A. P. Jones, *Phil. Trans. R. Soc. Lond. A*, 2001, **359**, 1961–1972.

21 A. P. Jones, A. G. G. M. Tielens, D. J. Hollenbach and C. F. McKee, *Astrophys. J.*, 1994, **433**, 797–810.

22 A. P. Jones, A. G. G. M. Tielens and D. J. Hollenbach, *Astrophys. J.*, 1996, **469**, 740–764.

23 S. Zhukovska, C. Dobbs, E. B. Jenkins and R. S. Klessen, *Astrophys. J.*, 2016, **831**, 147.

24 M. J. Michałowski, *Astron. Astrophys.*, 2015, **577**, A80.

25 R. McKinnon, P. Torrey and M. Vogelsberger, *Mon. Not. R. Astron. Soc.*, 2016, **457**, 3775–3800.

26 S. Zhukovska, H.-P. Gail and M. Trieloff, *Astron. Astrophys.*, 2008, **479**, 453–480.

27 B. T. Draine, In Cosmic dust-near and far: proceedings of a conference held at the Heidelberg Convention Center, Heidelberg, Germany, 8–12 September 2008, International Conference, Astronomical Society of the Pacific, San Francisco, 2009, pp. 453–472.

28 F. J. Molster, I. Yamamura, L. B. F. M. Waters, A. G. G. M. Tielens, T. de Graauw, T. De Jong, A. De Koter, K. Malfait, M. E. Van den Ancker, H. Van Winckel, R. H. M. Voors and C. Waelkens, *Nature*, 1999, **401**, 563–565.

29 S. Höfner and H. Olofsson, *Astron. Astrophys. Rev.*, 2018, **26**, 1–92.

30 S. A. Krasnokutski, G. Rouillé, C. Jäger, F. Huisken, S. Zhukovska and T. Henning, *Astrophys. J.*, 2014, **782**, 15.

31 J. S. Anderson, J. S. Ogden and M. J. Ricks, *Chem. Commun.*, 1968, 1585–1586.

32 J. W. Hastie, R. H. Hauge and J. L. Margrave, *Inorg. Chim. Acta*, 1969, **3**, 601–606.

33 J. S. Anderson and J. S. Ogden, *J. Chem. Phys.*, 1969, **51**, 4189–4196.

34 R. K. Khanna, D. D. Stranz and B. Donn, *J. Chem. Phys.*, 1981, **74**, 2108–2115.

35 W. C. Lu, C. Z. Wang and K. M. Ho, *Chem. Phys. Lett.*, 2003, **378**, 225–231.

36 P. V. Avramov, I. Adamovic, K.-M. Ho, C. Z. Wang, W. C. Lu and M. S. Gordon, *J. Phys. Chem. A*, 2005, **109**, 6294–6302.

37 E. F. van Dishoeck, *Annu. Rev. Astron. Astrophys.*, 2004, **42**, 119–167.

38 J. C. G. Martín and J. M. C. Plane, *Phys. Chem. Chem. Phys.*, 2011, **13**, 3764–3774.

39 S. D. Le Picard, A. Canosa, D. Reignier and T. Stoecklin, *Phys. Chem. Chem. Phys.*, 2002, **4**, 3659–3664.

40 D. Husain and P. E. Norris, *J. Chem. Soc., Faraday Trans. 2*, 1978, **74**, 93–105.

41 S. D. Le Picard, A. Canosa, G. Pineau des Forêts, C. Rebrion-Rowe and B. R. Rowe, *Astron. Astrophys.*, 2001, **372**, 1064–1070.

42 F. Dayou and A. Spielfiedel, *J. Chem. Phys.*, 2003, **119**, 4237–4250.

43 I. Adamovic and M. S. Gordon, *J. Phys. Chem. A*, 2004, **108**, 8395–8399.

44 F. Dayou, W.-Ü. L. Tchang-Brillet and M. Monnerville, *J. Chem. Phys.*, 2005, **123**, 084306.

45 R. Yamashiro, Y. Matsumoto and K. Honma, *J. Chem. Phys.*, 2008, **128**, 084308.

46 D. Yuan, S. Yu, W. Chen, J. Sang, C. Luo, T. Wang, X. Xu, P. Casavecchia, X. Wang, Z. Sun, D. H. Zhang and X. Yang, *Nat. Chem.*, 2018, **10**, 653–658.

47 D. Yuan, W. Chen, C. Luo, Y. Tan, S. Li, Y. Huang, Z. Sun, X. Yang and X. Wang, *J. Phys. Chem. Lett.*, 2020, **11**, 1222–1227.

48 D. Yuan, Y. Huang, W. Chen, H. Zhao, S. Yu, C. Luo, Y. Tan, S. Wang, X. Wang, Z. Sun and X. Yang, *Nat. Commun.*, 2020, **11**, 3640.

49 N. Balucani, D. Skouteris, G. Capozza, E. Segoloni, P. Casavecchia, M. H. Alexander, G. Capecchi and H.-J. Werner, *Phys. Chem. Chem. Phys.*, 2004, **6**, 5007–5017.

50 D. Skouteris, H.-J. Werner, F. J. Aoiz, L. Banares, J. F. Castillo, M. Menéndez, N. Balucani, L. Cartechini and P. Casavecchia, *J. Chem. Phys.*, 2001, **114**, 10662–10672.

51 T. Yang, J. Chen, L. Huang, T. Wang, C. Xiao, Z. Sun, D. Dai, X. Yang and D. H. Zhang, *Science*, 2015, **347**, 60–63.

52 Y. Xie, Y. Wang, W. Wang, D. Dai, Z. Sun, C. Xiao and X. Yang, *J. Phys. Chem. A*, 2020, **124**, 1266–1271.

53 Y.-r Xie, Y.-f Wang, W. Wang, T. Wang, D.-x Dai, C.-l Xiao and X.-m Yang, *Chin. J. Chem. Phys.*, 2020, **33**, 135–138.

54 S.-H. Lee, F. Dong and K. Liu, *J. Chem. Phys.*, 2006, **125**, 133106.

55 T. Wang, J. Chen, T. Yang, C. Xiao, Z. Sun, L. Huang, D. Dai, X. Yang and D. H. Zhang, *Science*, 2013, **342**, 1499–1502.

56 T. Yang, L. Huang, T. Wang, C. Xiao, Y. Xie, Z. Sun, D. Dai, M. Chen, D. Zhang and X. Yang, *J. Phys. Chem. A*, 2015, **119**, 12284–12290.

57 T.-g Yang, L. Huang, Y.-r Xie, T. Wang, C.-l Xiao, Z.-g Sun, D.-x Dai, D. H. Zhang and X.-m Yang, *Chin. J. Chem. Phys.*, 2015, **28**, 471.

19770 | *Phys. Chem. Chem. Phys.*, 2022, **24**, 19761–19772

This journal is © the Owner Societies 2022

58 L. Huang, Y.-r Xie, T.-g Yang, T. Wang, D.-x Dai, C.-l Xiao and X.-m Yang, *Chin. J. Chem. Phys.*, 2019, **32**, 72–76.

59 N. Balucani, P. Casavecchia, F. Aoiz, L. Bañares, J.-M. Launay, B. Bussery-Honvault and P. Honvault, *Mol. Phys.*, 2010, **108**, 373–380.

60 N. Balucani, G. Capozza, E. Segoloni, A. Russo, R. Bobbenkamp, P. Casavecchia, T. Gonzalez-Lezana, E. J. Rackham, L. Bañares and F. J. Aoiz, *J. Chem. Phys.*, 2005, **122**, 234309.

61 L. A. Pederson, G. C. Schatz, T.-S. Ho, T. Hollebeek, H. Rabitz, L. B. Harding and G. Lendvay, *J. Chem. Phys.*, 1999, **110**, 9091–9100.

62 N. Balucani, M. Alagia, L. Cartechini, P. Casavecchia, G. G. Volpi, L. A. Pederson and G. C. Schatz, *J. Phys. Chem. A*, 2001, **105**, 2414–2422.

63 N. Balucani, L. Cartechini, G. Capozza, E. Segoloni, P. Casavecchia, G. G. Volpi, F. J. Aoiz, L. Bañares, P. Honvault and J.-M. Launay, *Phys. Rev. Lett.*, 2002, **89**, 013201.

64 N. Balucani, P. Casavecchia, L. Banares, F. J. Aoiz, T. Gonzalez-Lezana, P. Honvault and J.-M. Launay, *J. Phys. Chem. A*, 2006, **110**, 817–829.

65 X. Liu, J. J. Lin, S. Harich, G. C. Schatz and X. Yang, *Science*, 2000, **289**, 1536–1538.

66 N. Balucani, P. Casavecchia, F. J. Aoiz, L. Banares, J. F. Castillo and V. J. Herrero, *Mol. Phys.*, 2005, **103**, 1703–1714.

67 S.-H. Lee and K. Liu, *Appl. Phys. B*, 2000, **71**, 627–633.

68 B. Maiti, G. C. Schatz and G. Lendvay, *J. Phys. Chem. A*, 2004, **108**, 8772–8781.

69 H. Yang, K.-L. Han, G. C. Schatz, S.-H. Lee, K. Liu, S. C. Smith and M. Hankel, *Phys. Chem. Chem. Phys.*, 2009, **11**, 11587–11595.

70 R. I. Kaiser, P. Maksyutenko, C. Ennis, F. Zhang, X. Gu, S. P. Krishtal, A. M. Mebel, O. Kostko and M. Ahmed, *Faraday Discuss.*, 2010, **147**, 429–478.

71 A. M. Thomas, B. B. Dangi, T. Yang, R. I. Kaiser, B.-J. Sun, T.-J. Chou and A. H. H. Chang, *Chem. Phys.*, 2019, **520**, 70–80.

72 A. M. Thomas, B. B. Dangi, T. Yang, R. I. Kaiser, L. Lin, T.-J. Chou and A. H. H. Chang, *J. Phys. Chem. Lett.*, 2018, **9**, 3340–3347.

73 G. O. Brink, *Rev. Sci. Instrum.*, 1966, **37**, 857–860.

74 N. R. Daly, *Rev. Sci. Instrum.*, 1960, **31**, 264–267.

75 P. S. Weiss, PhD Dissertation Thesis, University of California, 1986.

76 M. F. Vernon, PhD Dissertation Thesis, University of California, 1983.

77 H.-J. Werner, P. J. Knowles, G. Knizia, F. R. Manby, M. Schütz, P. Celani, W. Györffy, D. Kats, T. Korona, R. Lindh, A. Mitrushenkov, G. Rauhut, K. R. Shamasundar, T. B. Adler, R. D. Amos, A. Bernhardsson, A. Berning, D. L. Cooper, J. O. Deegan, A. J. Dobbyn, F. Eckert, E. Goll, C. Hampel, A. Hesselmann, G. Hetzer, T. Hrenar, G. Jansen, C. Köppl, Y. Liu, A. W. Lloyd, R. A. Mata, A. J. May, S. J. McNicholas, W. Meyer,

M. E. Mura, A. Nicklass, D. P. O'Neill, P. Palmieri, D. Peng, K. Pflüger, R. Pitzer, M. Reiher, T. Shiozaki, H. Stoll, A. J. Stone, R. Tarroni, T. Thorsteinsson, M. Wang and M. Welborn, *MOLPRO, Version 2019.2, A Package of Ab Initio Programs*, University of Cardiff, Cardiff, UK, 2019, https://www.molpro.net.

78 B. O. Roos, P. R. Taylor and P. E. M. Sigbahn, *Chem. Phys.*, 1980, **48**, 157–173.

79 F. Weigend and R. Ahlrichs, *Phys. Chem. Chem. Phys.*, 2005, **7**, 3297–3305.

80 H.-J. Werner and P. J. Knowles, *J. Chem. Phys.*, 1988, **89**, 5803–5814.

81 H. Prautzsch, W. Boehm and M. Paluszny, *Bézier and B-spline techniques*, Springer, Berlin, Heidelberg, 1st edn, 2002.

82 G. Van Rossum and F. L. Drake Jr, *Python 3 reference manual*, CreateSpace, Scotts Valley, CA, 2019.

83 P. J. Knowles and H.-J. Werner, *Chem. Phys. Lett.*, 1988, **145**, 514–522.

84 R. D. Levine, *Molecular Reaction Dynamics*, Cambridge University Press, Cambridge, 2005.

85 W. B. Miller, S. A. Safron and D. R. Herschbach, *Discuss. Faraday Soc.*, 1967, **44**, 108–122.

86 J. M. Ribeiro and A. M. Mebel, *Phys. Chem. Chem. Phys.*, 2017, **19**, 14543–14554.

87 M. W. Chase Jr, *J. Phys. Chem. Ref. Data, Monograph*, 1998, **9**, 1728–1885.

88 S. Yamauchi, *CODATA key values for thermodynamics*, Hemisphere Pub, 1976.

89 B. R. Lewis, L. Berzins, J. H. Carver and S. T. Gibson, *J. Quantum Spectrosc. Radiat. Transfer*, 1985, **33**, 627–643.

90 K. Raghavachari, G. W. Trucks, J. A. Pople and M. Head-Gordon, *Chem. Phys. Lett.*, 1989, **157**, 479–483.

91 A. J. C. Varandas, *J. Chem. Phys.*, 2000, **113**, 8880–8887.

92 K. Fukui, *J. Phys. Chem.*, 1970, **74**, 4161–4163.

93 S. Maeda, Y. Harabuchi, Y. Ono, T. Taketsugu and K. Morokuma, *Int. J. Quantum Chem.*, 2015, **115**, 258–269.

94 J. Ischtwan and M. A. Collins, *J. Chem. Phys.*, 1988, **89**, 2881–2885.

95 R. R. Zaari and S. A. Varganov, *J. Phys. Chem. A*, 2015, **119**, 1332–1338.

96 A. Farazdel and M. Dupuis, *J. Comput. Chem.*, 1991, **12**, 276–282.

97 D. G. Delgado, H. Olofsson, F. Kerschbaum, F. L. Schöier, M. Lindqvist and M. A. T. Groenewegen, *Astron. Astrophys.*, 2003, **411**, 123–147.

98 M. D. Allendorf, C. F. Melius, P. Ho and M. R. Zachariah, *J. Phys. Chem.*, 1995, **99**, 15285–15293.

99 J.-H. Chen, P. F. Goldsmith, S. Viti, R. Snell, D. C. Lis, A. Benz, E. Bergin, J. Black, P. Caselli, P. Encrenaz, E. Falgarone, J. R. Goicoechea, Å. Hjalmarson, D. Hollenbach, M. Kaufman, G. Melnick, D. Neufeld, L. Pagani, F. van der Tak, E. van Dishoeck and U. A. Yıldız, *Astrophys. J.*, 2014, **793**, 111.

100 S. Weinreb, A. H. Barrett, M. L. Meeks and J. C. Henry, *Nature*, 1963, **200**, 829–831.

101 J. Harju, A. Winnberg and J. G. A. Wouterloot, *Astron. Astrophys.*, 2000, **353**, 1065–1073.

102 A. Bieler, K. Altwegg, H. Balsiger, A. Bar-Nun, J.-J. Berthelier, P. Bochsler, C. Briois, U. Calmonte, M. Combi, J. De Keyser, E. F. van Dishoeck, B. Fiethe, S. A. Fuselier, S. Gasc, T. I. Gombosi, K. C. Hansen, M. Hässig, A. Jäckel, E. Kopp, A. Korth, L. L. Roy, U. Mall, R. Maggiolo, B. Marty, O. Mousis, T. Owen, H. Rème, M. Rubin, T. Sémon, C.-Y. Tzou, J. H. Waite, C. Walsh and P. Wurz, *Nature*, 2015, **526**, 678–681.

103 V. Taquet, K. Furuya, C. Walsh and E. F. van Dishoeck, *Mon. Not. R. Astron. Soc.*, 2016, **462**, S99–S115.

104 Y. F. Zhu and R. J. Gordon, *J. Chem. Phys.*, 1990, **92**, 2897–2901.

105 A. Stolow and Y. T. Lee, *J. Chem. Phys.*, 1993, **98**, 2066–2076.

106 J. A. Schmidt, M. S. Johnson and R. Schinke, *Proc. Natl. Acad. Sci. U. S. A.*, 2013, **110**, 17691–17696.

107 Z. Chen, F. Liu, B. Jiang, X. Yang and D. H. Parker, *J. Phys. Chem. Lett.*, 2010, **1**, 1861–1865.

108 F. Dayou, P. Larrégaray, L. Bonnet, J.-C. Rayez, P. N. Arenas and T. González-Lezana, *J. Chem. Phys.*, 2008, **128**, 174307.

109 T. Yang, A. M. Thomas, B. B. Dangi, R. I. Kaiser, A. M. Mebel and T. J. Millar, *Nat. Commun.*, 2018, **9**, 774.